Exact higher-order bulk-boundary correspondence of corner-localized states

Minwoo Jung [1,*] Yang Yu,[2] and Gennady Shvets[2,†]
[1]*Department of Physics, Cornell University, Ithaca, New York 14853, USA*
[2]*School of Applied and Engineering Physics, Cornell University, Ithaca, New York 14853, USA*

(Received 6 April 2021; revised 24 September 2021; accepted 22 November 2021; published 30 November 2021)

We demonstrate that the presence of a localized state at the corner of an insulating domain is not always a predictor nor a direct consequence of a certain nontrivial higher-order topological invariant, even though they appear to coexist in the same Hamiltonian parameter space. Our analysis of C_n-symmetric crystalline insulators and their multilayer stacks reveals that topological corner states are not necessarily correlated with other well-established higher-order boundary observables, such as fractional corner charge or filling anomaly. In a C_3-symmetric breathing Kagome lattice, for example, we show that the bulk polarization, which successfully predicts the fractional corner anomaly, fails to be the relevant topological invariant for zero-energy corner states; instead, these corner states are explained by the decoration of topological edges. Also, while the corner states at the interface between C_4-symmetric topological crystalline insulators and their trivial counterpart have long been reported to be the result of the bulk polarization of the lowest band, we reveal that such embedded corner states are trivial defect states. By refining several bulk-corner correspondences in two-dimensional topological crystalline insulators, our work motivates further development of rigorous theoretical grounds for associating the existence of corner states with higher-order topology of host materials.

DOI: 10.1103/PhysRevB.104.195437

I. INTRODUCTION

Bulk-boundary correspondence (BBC) lies at the heart of topological physics. BBC bridges abstract mathematical indices called topological invariants, which are calculated from band structures of a bulk material, to physical observables at its boundary. Early efforts in establishing BBC focused on boundaries of codimension 1 such as edges of two-dimensional (2D) materials or surfaces of three-dimensional (3D) materials [1–5]. Inspired by the discovery—both theoretical [6–11] and experimental [12–16]—of topological materials that feature gapless states at boundaries of codimension $d \geqslant 2$, efforts have recently been made to extend the framework of BBC to these higher-order topological phases [17–19].

The study of BBC sometimes takes the form of analytic case studies with a specific form of topological invariant [3,4,19], or relies on algebraic topology for generic classification of bulk and boundary Hamiltonians [1,2,5,17,18]. While the latter approach provides more comprehensive formulation of BBC than the former does, its concern does not aim further than identifying the classification group of Hamiltonian in certain symmetry classes, thereby evading the task of finding the actual topological invariants relevant to the boundary signatures. For example, the algebraic knowledge of "the homotopy group of unitary symmetry group is $\mathbb{Z}$ in 2D" [1,2] does not reveal the definition of a relevant bulk invariant nor the mechanism of how a certain invariant leads to boundary signature. In contrast, the BBC of the 2D unitary symmetry group was undoubtedly completed by the famous work by Thouless, Kohmoto, Nightingale, and denNijs [20] that provided an analytic derivation on the relationship between Chern number and the quantized Hall conductivity. Therefore, while the algebraic classification method allows an insightful start for the search of topological structures, rigorous BBC cannot be established without rigorous analytic studies that specifically address a certain pair of a bulk invariant and a boundary signature.

As the field of higher-order topological insulators (HOTIs) rapidly expanded, however, rigorous BBCs have often been replaced by an implicit assumption that it suffices to show merely that the boundary signatures (e.g., corner-localized states) "appear at the same time" with a bulk invariant by which the host bulk Hamiltonian can be characterized (e.g., bulk polarization). To be specific, the following prescriptive framework is widely used in the field of HOTIs [21–45]: (1) find a symmetry-protected bulk topological invariant of a given Hamiltonian model within a certain range of parameters, (2) uncover corner-localized states for the same parameters of the Hamiltonian as in (1), and (3) conflate (1) and (2) because both occur for the same parameters' range. Because correlation does not imply causation, the above procedure does not necessarily imply that the boundary signature has a topological origin. A physical explanation is necessary to establish the causal relationship between bulk invariants and the emergence of anomalous boundary properties. Otherwise, a topological nature of a boundary can be attributed to an irrelevant bulk invariant, or a trivial defect state can be mistaken for a topological one, thereby obscuring true BBCs.

*mj397@cornell.edu
†gshvets@cornell.edu

In this work, we address several cases of such weakly conjectured higher-order BBC, specifically in the context of corner-localized states and bulk polarization in 2D C_n-symmetric topological crystalline insulators (TCIs). By introducing the multilayer stacking construction of TCIs, inspired by Ref. [46], we clearly reveal that ZCSs in C_3-symmetric TCI (also known as breathing Kagome lattices) are not well correlated with the bulk polarization characterized by $\mathbb{Z}_3$, contrary to many previous works that claimed BBC between ZCS and bulk polarization in C_3-symmetric TCI [21–34]. We show that, at best, ZCSs in C_3-symmetric TCI can be understood as purely an edge effect associated with the $\mathbb{Z}_2$ composite Zak phase of chiral-symmetric edge bands.

Also, we discuss the issues with the corner states in the four-band C_4-symmetric TCI model. First, we clarify and complement the BBC regarding the ZCS in the open-boundary—i.e., terminated with vacuum—system reported by Refs. [47,48]. We show that, for an unambiguous BBC, it is necessary to introduce a half corner charge index at the half filling despite the lack of band gap at zero energy. It turns out that the corner charge index defined at half filling (the first and the second band altogether) becomes a proper bulk invariant responsible for ZCSs under the presence of the chiral symmetry and the reflection symmetry. Second, we reveal that the corner states, which appear at 90°-cornered interfaces between topological and trivial domains, are trivial defect states without any topological origin, while many previous studies regarding this C_4-symmetric TCI model [35–43] suggested BBC between these embedded corner states and the bulk polarization of the lowest energy band because they appear at the band gap right above the lowest band. The underlying theory work [35] of those studies explicitly claimed such correspondence between the embedded corner states at the embedded-boundary and the ZCS in the open-boundary system. However, we show that the counterpart zero-energy state in the embedded-boundary system exists as a state delocalized in the outer domain, and the trivial embedded corner states at the band gap above the lowest band can be independently made to disappear by a local perturbation that respects all essential symmetries of the system (C_{4v} and chiral symmetry). These examples clearly demonstrate that a precise formulation of BBC requires more than simply identifying the phase diagrams of a bulk invariant and a boundary state.

To set some good examples on the contrary, we briefly review several well-established BBCs. A classic example is the forementioned correspondence between the Hall conductivity (a surface effect) and Chern number (a bulk topological index). The two are directly related through an analytic expression [20]. Because conduction cannot occur in an insulating bulk, nonzero Hall conductivity in a Chern insulator must indicate metallic channels on its edge or, in other words, gapless edge states [49]. Another analytically straightforward BBC is found between fractional edge charge and bulk polarization in a one-dimensional (1D) TCI [50], i.e., the Su-Schrieffer-Heeger (SSH) model. Recent works [11,46] established higher-order versions of similar correspondences in 2D TCIs by explicitly constructing bulk invariants for fractional corner charges. Even though these boundary anomalies in the form of fractional charge excess/deficit have yet to be incorporated in the framework of the algebraic classification

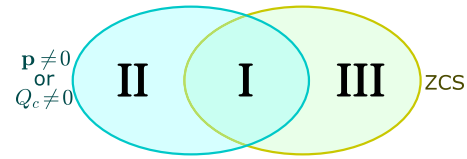

FIG. 1. Venn diagram classification of crystalline insulators in regard to the existence of nonzero $\mathbf{p}$ or Q_c and the existence of ZCSs. (I) A class of models that support both nontrivial bulk higher-order topology and ZCSs, (II) support nonzero $\mathbf{p}$ or Q_c only, but no ZCSs, and (III) support ZCSs despite trivial bulk topology.

method [18], they have recently attracted attention as alternative observables of higher-order topology [51].

Our key message is that, unlike the above-mentioned nonvanishing Chern number being a necessary and sufficient condition for the existence of gapless edge states under a clear BBC [20,49], nontrivial bulk polarization $\mathbf{p}$ or secondary topological index for corner charge Q_c [46] are not always sufficient or necessary for the existence of corner *states*, even though they appear to coexist in some systems. As recently pointed out [46,51], the observables in a straightforward BBC with $\mathbf{p}$ or Q_c are fractional corner or edge *charge* anomalies. Therefore, the treatment of BBC regarding the corner states requires extra caution. The Venn diagram shown in Fig. 1 schematically illustrates our key result: a ZCS might not exist despite nontrivial $\mathbf{p}$ and Q_c (classification set II) or a ZCS can arise despite vanishing $\mathbf{p}$ and Q_c (classification set III). Figures 2(a) and 2(b) depict C_3- and C_4-symmetric crystalline insulators, respectively, that are used as exemplary models to support our key results, and Table I summarizes various C_3- and C_4-symmetric Hamiltonian models according to each classification category defined in Fig. 1. In Table I and Fig. 1, C_3-symmetric models that belong to set I are $(6\mathbb{N}-5)$- or $(6\mathbb{N}-1)$-layer stacking of the $h^{(3)}$ model given in Fig. 2(a) with $|t| < |\lambda|$, as these stacked models possess nonzero bulk polarization and ZCSs. $(6\mathbb{N}-4)$- or $(6\mathbb{N}-2)$-layer stacking of the $h^{(3)}(|t| < |\lambda|)$ model belong to set II, as these stacked models possess nonzero $\mathbf{p}$ but do not exhibit ZCSs. On the contrary, $(6\mathbb{N}-3)$-layer stacking of the $h^{(3)}(|t| < |\lambda|)$ model belong to set III, as these stacked models possess ZCSs despite vanishing $\mathbf{p}$. Therefore, it is clear that the BBC for ZCSs C_3-symmetric models cannot be explained by the bulk polarization. For C_4-symmetric models, the $h^{(4)}$ model given

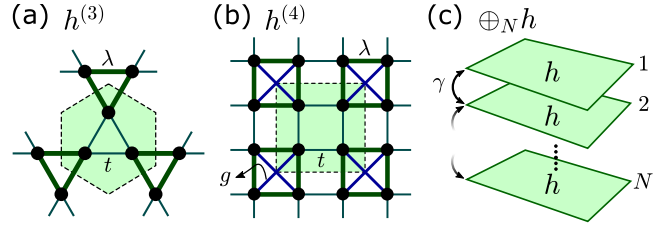

FIG. 2. (a) C_3-symmetric crystalline insulator model $h^{(3)}$; t and λ are the nearest-neighbor coupling within and across unit cells, respectively. (b) C_4-symmetric crystalline insulator model $h^{(4)}$; g is the next-nearest-neighbor coupling across diagonally adjacent unit cells. (c) N-layer stacking of a Hamiltonian model h, $\oplus_N h$; γ denotes the interlayer coupling strength.

TABLE I. Hamiltonian models of C_3- and C_4-symmetric insulators for each classification set introduced in Fig. 1.

	C_3-symm. models	C_4-symm. models
I	$\oplus_{1,5,7,11,\ldots} h^{(3)}(\lvert t\rvert < \lvert\lambda\rvert)$	$h^{(4)}(\lvert t\rvert < \lvert\lambda\rvert; g = 0)$
II	$\oplus_{2,4,8,10,\ldots} h^{(3)}(\lvert t\rvert < \lvert\lambda\rvert)$	$h^{(4)}(\lvert t\rvert < \lvert\lambda\rvert; g \neq 0)$
III	$\oplus_{3,9,15,\ldots} h^{(3)}(\lvert t\rvert < \lvert\lambda\rvert)$	

in Fig. 2(b) with $|t| < |\lambda|$ and $g = 0$ possesses ZCSs along with nonzero $\mathbf{p}$ and Q_c, thereby belonging to set I. But, the $h^{(4)}(|t| < |\lambda|)$ model with nonzero g loses the ZCSs due to the lack of chiral symmetry despite carrying the same $\mathbf{p}$ and Q_c to the vanishing g case. Each Hamiltonian model element in Table I is discussed in more details in the following sections.

II. STACKING OPERATION

We introduce the stacking operation $\oplus$ between two crystalline insulators h_1 and h_2, as defined in Ref. [46]:

$$h_1 \oplus h_2 = \begin{bmatrix} h_1 & \gamma \\ \gamma^\dagger & h_2 \end{bmatrix}, \tag{1}$$

where γ describes the nearest-neighbor coupling between adjacent layers. The strength of interlayer coupling is set to be reasonably small so that the shared band gap of $h_{1,2}$ is not closed. We denote an N layer stack of h as $\oplus_N h$, as depicted in Fig. 2(c). This operation allows us to easily access other topologically distinct phases, as the topological indices of a stacked insulator are simply given as an addition of those in each layer [46]; for example,

$$\mathbf{p}_{h_1 \oplus h_2} \equiv \mathbf{p}_{h_1} + \mathbf{p}_{h_2} \ (\mathrm{mod}\ \{\mathbf{R}\}), \tag{2}$$

where the composite polarization $\mathbf{p}$ (normalized to a unit charge) is evaluated in each model for all bands below the shared band gap of interest, and is given in modulo the set of primitive lattice vectors $\{\mathbf{R}\}$. The same relation holds for Q_c as well in modulo unit charge. The stacking operation defined here in Eq. (1) and its property in Eq. (2) turn out to be extremely useful in constructing case models that belong to each category of the Venn diagram in Fig. 1, especially for C_3-symmetric crystalline insulators as shown in Table I.

III. ZCS IN C_3-SYMMETRIC TCI AS BOUNDARY TOPOLOGICAL EFFECTS

Now, we consider the example model $h^{(3)}$ in Fig. 2(a), also known as a breathing Kagome lattice, with threefold rotational C_3 symmetry. When the nearest-neighbor coupling strengths across unit cells, λ, are greater than those within unit cells, t, the considered model is known to carry a ZCS emerging at every 60°-angled corner of a type with a single cornermost sublattice, as depicted in Fig. 3(a) (another type of 60°-angled corner with two cornermost sublattices does not support ZCSs). The same condition $|t| < |\lambda|$ produces nonzero bulk polarization $\mathbf{p}_{(1)} = \frac{2}{3}\mathbf{R}_1 + \frac{2}{3}\mathbf{R}_2$ in the lowest energy band [22–24,46], which is separated from the second and third bands by a band gap; see Fig. 3(b). Figure 3(c) illustrates that each Wannier center is displaced from the origin of each unit cell by bulk polarization vector $\mathbf{p}_{(1)}$, and therefore located

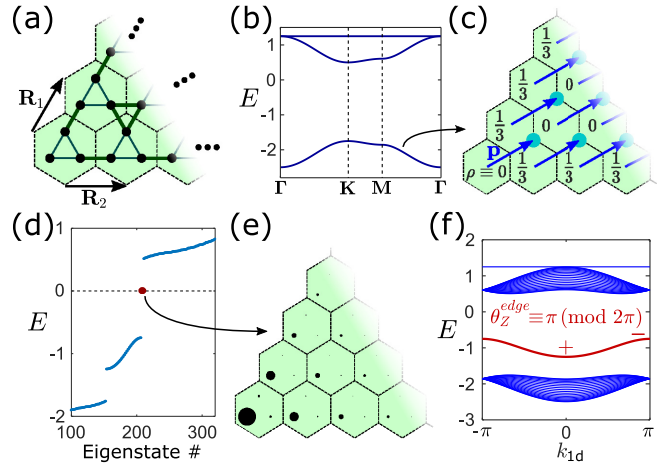

FIG. 3. (a) 60°-angled corner with a single cornermost sublattice. (b) Band structure of $h^{(3)}$; $t = -0.25$ and $\lambda = -1$. (c) Charge distribution around a 60°-angled corner at $\frac{1}{3}$ filling (up to the first band only); turquoise circles denote the Wannier centers displaced by $\mathbf{p} = \frac{2}{3}\mathbf{R}_1 + \frac{2}{3}\mathbf{R}_2$ from the unit cell centers. (d) Eigenspectra of a finite-sized system (190 unit cells) with open boundaries of triangular termination like in (a); corner-localized modes are highlighted as dark red dots. (e) Field profile of a ZCS; the area of black circles are proportional to the wave function amplitude. (f) Edge dispersion of nanoribbon structure with an edge termination like one of the edges in (a); the edge localized band is colored red along with its inversion eigenvalues at high symmetry points.

at the junction vertice of three adjacent hexagonal unit cells. Thus, in the limit of $|t| \ll |\lambda|$ (i.e., the localization length of Wannier function is much smaller than the unit cell size), a unit cell gains fractional charge of $\frac{1}{3}$ from each Wannier center in contact, when the lowest energy band is occupied. For example, the cornermost unit cell carries no charge $\rho = 0$ as there is no Wannier center in contact, each unit cell along both edges carries a fractional charge of $\rho = \frac{1}{3}$ as there is a Wannier center in contact, and each unit cell in the bulk carries a whole charge $\rho \equiv 0$ (mod 1) as there are three Wannier centers in contact. From this observation, it has been recently established that nonzero bulk polarization in $h^{(3)}$ gives rise to a higher-order topological observable called fractional corner anomaly (FCA) $\phi = \rho_{\mathrm{corner}} - \rho_{\mathrm{edge1}} - \rho_{\mathrm{edge2}} = 0 - \frac{1}{3} - \frac{1}{3} \equiv \frac{1}{3}$ (mod 1) [51]. Note that FCA is nonvanishing even in the absence of corner charge $\rho_{\mathrm{corner}} = Q_c$.

Regarding the existence of a ZCS shown in Figs. 3(d) and 3(e), many previous works [21–34] labeled the ZCS to be *higher-order-topological* merely due to its coexistence with the bulk polarization $\mathbf{p}_{(1)}$ in the Hamiltonian parameter space ($|t| < |\lambda|$). This conjecture, however, is disproved by our analysis of multilayer stacking constructions of $\oplus_{1,2,3,\ldots} h^{(3)}(|t| < |\lambda|)$ described below. Instead, we prove that the existence of a ZCS is a result of topological Zak phase of the edge localized band. Figure 3(f) shows the band dispersion of 1D-periodic nanoribbon structure terminated by an edge shown in Fig. 3(a), where the red line denotes an edge-localized band. This edge band carries the inversion eigenvalues of $+1$ at $k_{1d} = 0$ and -1 at $k_{1d} = \pi$, thereby featuring a Zak phase of $\theta_Z^{\mathrm{edge}} = \pi$ [50] (or polarization of $\frac{1}{2}$

[11]). The energy dispersion of this band follows $E(k_{1d}) = -\sqrt{t^2+\lambda^2+2t\lambda\cos(k_{1d})}$, which is reminiscent of a 1D chiral-symmetric SSH chain [50]. In fact, the chiral partner band of this edge band in Fig. 3(d) does not stand out since it is hybridized with other bulk bands at positive energy. The detailed discussion on how this edge-localized band is exactly mapped onto a 1D chiral-symmetric SSH chain is provided in the Appendix.

In what follows, we analyze the multilayer stacks of $h^{(3)}(|t|<|\lambda|)$ to show that the existence of ZCSs of a breathing Kagome lattice is correlated with neither finite bulk polarization nor with finite FCA. Such correlation has been widely assumed because the existence conditions $|t|<|\lambda|$ for ZCSs and nonzero $\mathbf{p}$ appear to coincide with each other [22–24]. Bilayer and trilayer stacks of $h^{(3)}(|t|<|\lambda|)$, according to Eq. (2), carry the bulk polarization of $\mathbf{p}_{(2)} \equiv 2\mathbf{p}_{(1)} \equiv \frac{1}{3}\mathbf{R}_1 + \frac{1}{3}\mathbf{R}_2$ and $\mathbf{p}_{(3)} \equiv 3\mathbf{p}_{(1)} \equiv 0$, respectively. Thus, based on their bulk polarization, $\oplus_2 h^{(3)}$ is classified as topologically nontrivial and $\oplus_3 h^{(3)}$ as trivial. This distinction will indeed physically manifest in their FCA; $\phi = \frac{2}{3}$ for $\oplus_2 h^{(3)}$ and $\phi = 0$ for $\oplus_3 h^{(3)}$. Therefore, if the presence of a ZCS were predicated on the finite FCA, we would expect that $\oplus_2 h^{(3)}$ should possess a ZCS, while $\oplus_3 h^{(3)}$ should not. Remarkably, the opposite is true, as observed from Figs. 4(a) and 4(b). Furthermore, the quad-layer stack $\oplus_4 h^{(3)}$ shares exactly the same bulk polarization $\mathbf{p}_{(4)} \equiv 4\mathbf{p}_{(1)} \equiv \mathbf{p}_{(1)}$ and FCA $\phi = \frac{1}{3}$ with the original monolayer structure $h^{(3)}$ that supports ZCSs, but $\oplus_4 h^{(3)}$ does not support a ZCS as shown in Fig. 4(c).

On the other hand, the composite Zak phase of the edge-localized bands in those structures, as shown in Figs. 4(d)–4(f), predicts well the existence of ZCSs. In the presence of multiple bands below a certain band gap of interest, the existence of a midgap boundary/dislocation state in 1D systems is determined by the composite Zak phase of all bands below the band gap [52,53]. Thus we find that a stack with an even number of layers features vanishing $\theta_Z^{\text{edge}} = 0 \pmod{2\pi}$ and a stack with an odd number of layers has nontrivial $\theta_Z^{\text{edge}} = \pi$. Accordingly, we observe the ZCSs in odd-layer stacks, but not in even-layer stacks. We note that there exist two corner-localized states in the bilayer stack structure as well, but they are not pinned at zero energy. Their spectral positions are at $E = \pm\gamma$, where γ is the interlayer coupling strength. Consequently, these corner states are not spectrally stable against perturbations in γ (e.g., vertical compression). Similarly, the trilayer stack also carries two spectrally unstable corner states at $E = \pm\sqrt{2}\gamma$ other than the ZCS. The spectral shifts of these corner states with respect to the change in γ is drawn in Fig. 4(g).

In general, $\oplus_N h^{(3)}(|t|<|\lambda|)$ carries N corner-localized states and one of them becomes a ZCS with topological spectral pinning, when N is an odd number. Therefore, it is clear that the existence of ZCSs is determined not by $\mathbb{Z}_3$ bulk polarization, but by $\mathbb{Z}_2$ edge band Zak phase. To be specific, a corner acts as a termination to each of two edge-localized SSH chains, and each topological ($\theta_Z^{\text{edge}} = \pi$) SSH chain is expected to support a zero-energy state localized at the termination: $|v_1\rangle = \sum_{n,m\geqslant 0}[\beta_1^{b\to e}]^n[\beta_1^{e\to c}]^m |A; n\mathbf{R}_1 + m\mathbf{R}_2\rangle$ and $|v_2\rangle = \sum_{n,m\geqslant 0}[\beta_2^{b\to e}]^n[\beta_2^{e\to c}]^m |A; n\mathbf{R}_2 + m\mathbf{R}_1\rangle$. Here, A is the sublattice index of the cornermost sublattice, $|A;\mathbf{R}\rangle$ is the basis vector that occupies the sublattice A in the unit cell located at position $\mathbf{R}$, and $\beta_i^{b\to e}/\beta_i^{e\to c}$ is the bulk-to-edge/edge-to-corner localization factor as depicted in Fig. 4(h). It turns out that these two localized states from each edge coalesce $|v_1\rangle = |v_2\rangle$, as the bulk-to-edge localization factor of an edge matches exactly to the edge-to-corner localization factor of the other edge: $\beta_1^{b\to e} = \beta_2^{e\to c} = -t/\lambda$ and $\beta_2^{b\to e} = \beta_1^{e\to c} = -t/\lambda$.

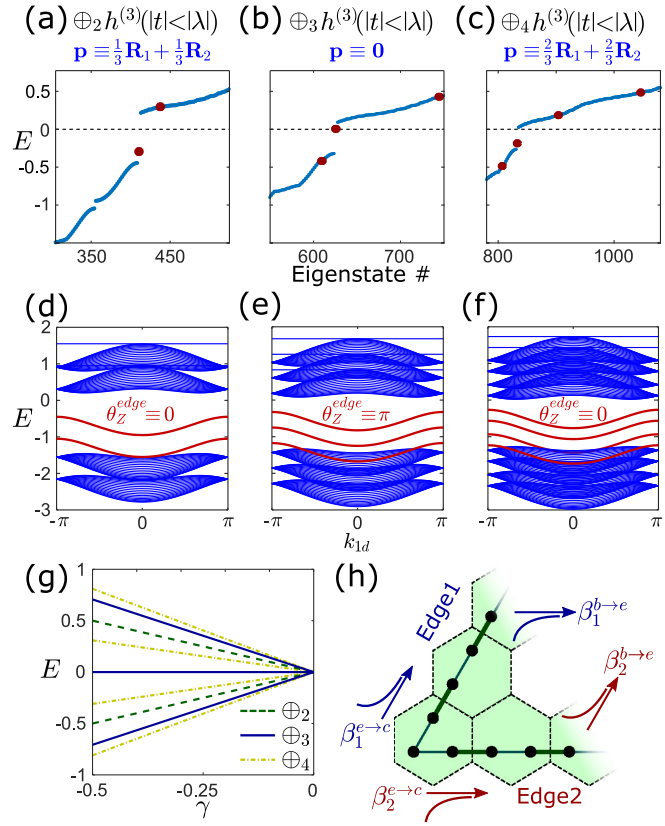

FIG. 4. (a)–(c) Eigenspectra of a finite-sized system—190 unit cells as in Fig. 3(d)—of the bi-, tri-, and quad-layer stacked structures of $h^{(3)}$ ($t = -0.25$, $\lambda = -1$), respectively, with the interlayer coupling strength of $\gamma = -0.3$; corner-localized modes are highlighted as dark red dots. (d)–(f) Edge dispersion of nanoribbon structure of bi-, tri-, and quad-layer structures, respectively, as in Fig. 3(f); the composite Zak phases of the edge-localized bands (dark red) are denoted together. (g) Energies of all corner-localized states in bi- (dashed green), tri- (solid blue), and quad-layer (dot/dashed orange) structures as a function of γ. (h) At the corner, each of two edge-localized SSH chains ($i = 1, 2$) supports a zero-energy termination-localized state, where it is localized along the edge with the edge-to-corner localization factor $\beta_i^{e\to c}$ and localized with respect to the bulk with the bulk-to-edge localization factor $\beta_i^{b\to e}$. These two states coalesce to each other as $\beta_1^{b\to e} = \beta_2^{e\to c}$ and $\beta_2^{b\to e} = \beta_1^{e\to c}$, giving rise to a ZCS to the bulk Hamiltonian.

Lastly, we show that ZCSs still arise in a breathing Kagome lattice, when there is no bulk crystalline symmetry. Figure 5 clearly demonstrates that ZCSs are well preserved even though hopping strengths are all different for three sides and C_3-rotational and mirror symmetries are broken. Like this case where we observe edge-induced corner states without any connection to bulk properties, several recent works

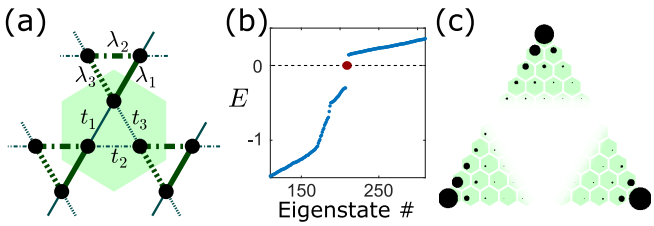

FIG. 5. (a) Breathing Kagome lattice without any bulk crystalline (C_3 nor mirror) symmetries. (b) Eigenspectra of a finite-sized system—190 unit cells as in Fig. 3(d)– -with $t_1 = -0.5$, $\lambda_1 = -0.9$, $t_2 = -0.3$, $\lambda_2 = -1$, $t_3 = -0.1$, and $\lambda_3 = -0.4$. (c) Field profiles of ZCSs at each corner.

have similarly identified higher-order topological signatures stemming from boundary (not bulk) topology in the language of decoration subgroups [18] or embedded topological insulators [54].

IV. ZCS IN C_4-SYMMETRIC TCI WITH OPEN BOUNDARIES

Next, we consider the example model $h^{(4)}$ in Fig. 2(b) with fourfold rotational C_4 symmetry. Before we address the main issue of the embedded corner states that arise at the 90°-cornered embedded-boundary between the trivial ($|t| > |\lambda|$) and the topological ($|t| < |\lambda|$) domains, we first investigate the ZCS in the open-boundary system. For the ZCS in the open-boundary system of the C_4-symmetric TCI model $h^{(4)}(|t| < |\lambda|; g = 0)$, we establish an alternative BBC that complements the study presented in Refs. [47,48]. References [47,48] report that the reflection symmetry (thus C_{4v} symmetry along with the underlying rotational symmetry) and the chiral symmetry prevent the inseparable hybridization of the corner state and the bulk states at the zero energy, allowing the well-localized ZCS to exist as a bound state in continuum. The proof given in Ref. [47] starts by assuming the existence of a zero-energy eigenstate that consists of a corner-localized part and a bulk part, and proves that the bulk part is trivially separable under C_{4v} and chiral symmetries. Their initial assumption of the existence of such a zero-energy eigenstate with corner-concentrated (even though not fully localized) distribution, however, eventually relies on the phenomenological observation of the corner density of state being peaked at the zero energy, rather than being unambiguously explained through topological effects, for the following reasons.

As shown in Fig. 6(a), the $h^{(4)}(|t| < |\lambda|; g = 0)$ model has no band gap at half filling; in other words, the second and the third band touch at zero energy. Thus the higher-order topology of this system has been described by the corner charge index of the first band, the middle two bands together, and the fourth band: $Q_c = (-\frac{1}{4}, \frac{1}{2}, -\frac{1}{4})$ mod 1. An important thing to note is that this topological corner charge index is always given in modulo 1, and $Q_c = \frac{1}{2}$ can manifest either as an excess charge of $+\frac{1}{2}$ or as a deficit charge of $-\frac{1}{2}$ in the open-boundary system. The presence of a corner-localized state can be unambiguously predicted only with the prior knowledge that all Q_c manifests as a deficit charge, thereby requiring a whole charge compensation by a corner state.

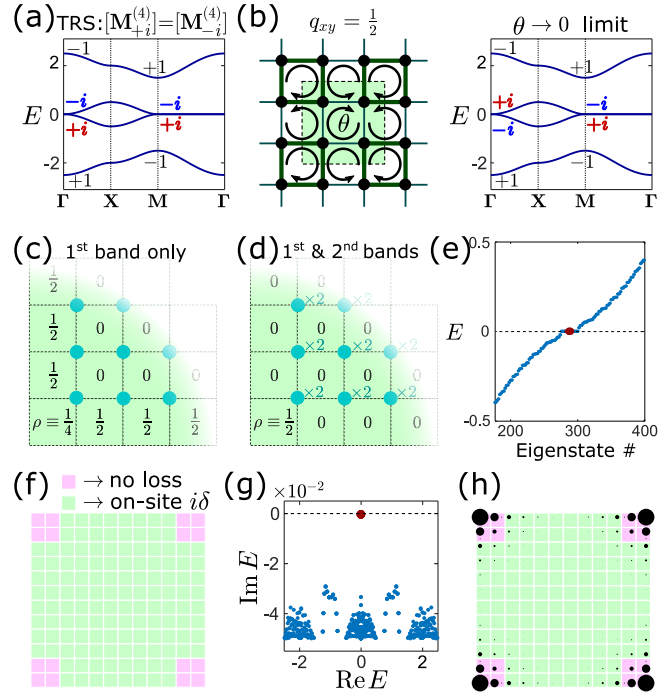

FIG. 6. (a) Band structure of $h^{(4)}$ along with C_4-rotation eigenvalues at Γ and M; $t = -0.25$, $\lambda = -1$, and $g = 0$. (b) Staggering phase flux of θ realizes a quadrupole insulator, and the same structure in (a) is viewed as a zero-flux limit ($\theta \to 0$) of a quadrupole insulator; the C_4-rotation eigenvalues at Γ and M for the second and third bands are assigned differently. (c) Charge distribution around a corner at quarter filling (the first band only); turquoise circles are Wannier centers. (d) Charge distribution around a corner at half filling (up to the second band); two Wannier centers are overlapping at each position. (e) Eigenspectra of a finite-sized system with open boundaries (12 by 12 unit cells); the corner modes are marked as dark red dots. (f) A uniform on-site loss of $\delta = -0.05$ was applied to a open-boundary domain of 12×12 unit cells except at each 2×2 corner unit cell. (g) Resulting eigenvalues in a complex energy plane. (h) Field profile of the corner modes marked as dark red dots in (f) and (h).

Since the middle two bands are grouped together, however, the bit of information $Q_c = \frac{1}{2}$ itself cannot tell any specific arrangement of eigenstates at the zero energy.

Even with the chiral symmetry, at best we know that the half charge of two middle bands should be split into two quarters with respect to the zero energy, but still, before diagonalizing the finite system, there is no way to predict whether the split quarter charge for the second and the third bands will be $-\frac{1}{4}$ or $+\frac{1}{4}$ mod 1. If the split charges are $-\frac{1}{4}$—$Q_c = (-\frac{1}{4}, -\frac{1}{4}, -\frac{1}{4}, -\frac{1}{4})$—under the chiral symmetry, all Q_c need to manifest as charge deficits. Otherwise, the charge neutrality of the entire system cannot be met due to a pair (by chiral symmetry) of charge excess of $+\frac{3}{4}$; there will be $+\frac{3}{4} \times 2 - \frac{1}{4} \times 2 = +1$ excess charge, even if the other pair comes in the deficit of $-\frac{1}{4}$. Thus, in this case, a ZCS is guaranteed. If the split charges are $+\frac{1}{4}$—$Q_c = (-\frac{1}{4}, +\frac{1}{4}, +\frac{1}{4}, -\frac{1}{4})$—under the chiral symmetry, however, a ZCS cannot exist. Therefore, the presence of the ZCS cannot be predicted directly out of $Q_c = (-\frac{1}{4}, \frac{1}{2}, -\frac{1}{4})$ mod 1, as there is the latter possibility.

In order to resolve this ambiguity, we demonstrate that a half corner charge $Q_c = \frac{1}{2}$ is well defined at half filling for the first and the second band considered together, even though the system is gapless at zero energy between the second and the third band. In a time-reversal- and C_4-symmetric crystalline insulator, the following expressions can be used to determine its topological indices [46]:

$$\mathbf{p} = \tfrac{1}{2}\big[\mathbf{X}^{(2)}_{+1}\big](\hat{\mathbf{x}} + \hat{\mathbf{y}}) \ (\mathrm{mod}\ \{\hat{\mathbf{x}}, \hat{\mathbf{y}}\}), \tag{3a}$$

$$Q_c = \tfrac{1}{4}\big(\big[\mathbf{X}^{(2)}_{+1}\big] + 2\big[\mathbf{M}^{(4)}_{+1}\big] + 3\big[\mathbf{M}^{(4)}_{+i}\big]\big) \ (\mathrm{mod}\ 1), \tag{3b}$$

where $[\mathbf{k}^{(n)}_p] \equiv \#\mathbf{k}^{(n)}_p - \#\mathbf{\Gamma}^{(n)}_p$, and $\#\mathbf{k}^{(n)}_p$ refers to the number of eigenstates with C^n-rotation eigenvalue p at a C^n-rotational invariant momentum $\mathbf{k}$. The eigenstates are counted from the lowest propagation band up to the band of interest. For example, in $h^{(4)}(|t| < |\lambda|; g = 0)$, the C_2-rotation eigenvalues are $(-1, +1, +1, -1)$ at $\mathbf{X}$ and $(+1, -1, -1, +1)$ at $\mathbf{\Gamma}$ in order from the lowest band to the fourth band. Then, we get $[\mathbf{X}^{(2)}_{+1}] = \#\mathbf{X}^{(2)}_{+1} - \#\mathbf{\Gamma}^{(2)}_{+1} = 0 - 1 = -1$ for the lowest band only and $[\mathbf{X}^{(2)}_{+1}] = 1 - 1 = 0$ for the first two bands together. Thus, according to Eq. (3a), the lowest band carries a nonzero bulk polarization of $\mathbf{p} = \frac{1}{2}(\hat{\mathbf{x}} + \hat{\mathbf{y}})$, but the first two bands together feature vanishing polarization $\mathbf{p} = \mathbf{0}$.

Figure 6(a) depicts the band structure of the $h^{(4)}(|t| < |\lambda|; g = 0)$ model along with C_4-rotation eigenvalues at $\mathbf{M}$ and at $\mathbf{\Gamma}$. At $\mathbf{M}$ and $\mathbf{\Gamma}$, the second and third bands are degenerate at zero energy. As these degenerate modes have different eigenvalues $\pm i$, there arises an ambiguity of whether we assign $+i$ or $-i$ to the C_4-rotation eigenvalue of the second band. This ambiguity, however, can be lifted up partially by the time-reversal symmetry, which enforces $[\mathbf{M}^{(4)}_{+i}] = [\mathbf{M}^{(4)}_{-i}]$ (see the Supplemental Material of Ref. [46]), that we should choose the same values at $\mathbf{M}$ and at $\mathbf{\Gamma}$. Without loss of generality, $-i$ is assigned to the second band, see Fig. 6(a), which gives $[\mathbf{M}^{(4)}_{+i}] = 1 - 1 = 0$ for the first two bands. Then, along with $[\mathbf{X}^{(2)}_{+1}] = 0$ and $[\mathbf{M}^{(4)}_{+1}] = -1$, Eq. (3b) yields a half corner charge $Q_c = \frac{1}{2}$ for the first two bands.

Another way of interpreting this half charge is to consider this C_4-symmetric TCI model as a quadrupole insulator in a zero flux limit. A phase flux of θ can be achieved by complex tight-binding parameters $[t, \lambda] \to [t, \lambda] \times e^{+i\theta/4} (\times e^{-i\theta/4})$ for hopping along (against) the direction of arrows illustrated in Fig. 6(b). Any finite phase flux upon a cyclic hopping opens a complete band gap between the second and the third band, while maintaining the chiral symmetry [16]. In this setting, the C_4-rotation eigenvalue of the second band at $\mathbf{M}$, $+i$, is different from that at $\mathbf{\Gamma}$, $-i$, as shown in Fig. 6(c). While we cannot apply Eq. (3) any longer as the time-reversal symmetry is broken due to the finite flux, the quadrupole moment q_{xy} can be evaluated as

$$e^{i2\pi q_{xy}} = r^+_4(\mathbf{M}) r^+_4(\mathbf{\Gamma})^* = r^-_4(\mathbf{M}) r^-_4(\mathbf{\Gamma})^*, \tag{4}$$

where $r^{\pm}_4(\mathbf{k})$ is the C_4-rotation eigenvalue at $\mathbf{k} = \mathbf{M}/\mathbf{\Gamma}$ that satisfies $r^{\pm}_4(\mathbf{k})^2 = \pm 1$ [11,55]. From Fig. 5(c), we get $r^+_4(\mathbf{M}) = -1$, $r^+_4(\mathbf{\Gamma}) = +1$, $r^-_4(\mathbf{M}) = +i$, $r^-_4(\mathbf{\Gamma}) = -i$, and therefore $q_{xy} = Q_c = \frac{1}{2}$ [11].

Figure 6(c) shows the location of Wannier centers $\mathbf{p} = \frac{1}{2}(\hat{\mathbf{x}} + \hat{\mathbf{y}})$ and the resulting charge distribution (in modulo unit charge) at quarter filling (when the lowest energy band is filled) in the limit of $|t| \ll |\lambda|$ [46]. This quarter-filled configuration features edge charge density of $\frac{1}{2}$ per unit cell and FCA of $\phi = -\frac{1}{4}$ [51]. At half filling (when the first two bands are filled), we have provided two different perspectives—(1) enforcing time-reversal symmetry or (2) treating the system as a time-reversal-broken quadrupole insulator with infinitesimal band gap—that a corner charge index $Q_c = \frac{1}{2}$ can still be well-defined despite the lack of a band gap at zero energy. The resulting charge distribution at half filling (up to the second band) drawn in Fig. 6(d) shows a half corner charge and vanishing edge charge, as two overlapping Wannier centers from the first and second bands cancel the contribution to bulk polarization from each other.

Now that we have established a proper invariant $Q_c = \frac{1}{2}$ at half filling, we investigate the crucial role of the chiral symmetry at half filling for the existence of ZCSs. It is well studied in various systems [7,8,11,13–16,46,56] that the combination of a half fractional corner charge and the chiral symmetry guarantees a ZCS. If the bands below zero energy carry a half charge at a corner, the chiral symmetry ensures that the bands above zero energy also carry a half charge at the corner. Since the integration of the local density of states over energy must be equal to the number of bands at each unit cell (i.e., charge neutrality), the fractional corner charge in this case cannot be a charge excess as it implies that the integration at the corner unit cell exceeds the number of bands. Thus two half charge deficits, each from the lower and the upper bands, requires the existence of a corner state to compensate for a total whole charge deficit, and this corner state should be pinned at zero energy due to the chiral symmetry. This BBC based on $Q_c = \frac{1}{2}$ at half filling and the chiral symmetry does not leave any ambiguity that we discussed in the beginning of this section regarding the BBC based on the lumped treatment of the second and the third band.

We note that, due to the lack of band gap at zero energy, the reflection symmetry (C_{4v}) is additionally required to ensure that the predicted ZCS is immune to inseparable hybridization with the bulk states at the zero energy [47]. Without the reflection symmetry, even though our BBC still predicts the existence of a set of corner-loaded states at or around zero energy that compensates the corner charge deficit, these states may leak into the bulk continuum. Also, our approach to define a topological invariant at the half filling works only because the second and the third band simply touch each other at zero energy and do not overlap with each other in a finite energy range. This nonoverlapping band touch is in fact ensured by the chiral symmetry, which enforces the energy range of the second (third) band to be strictly less (greater) than or equal to zero energy.

The chiral symmetry in C_4-symmetric TCI is given as $S = \mathrm{diag}[1, -1, 1, -1]$, where the four sublattices are indexed in a clockwise order, and its presence $Sh^{(4)}S^{-1} = -h^{(4)}$ gives rise to a band structure that is mirror symmetric with respect to the zero energy as shown in Figs. 6(a) and 6(b). Since we have a half-corner charge and the chiral symmetry, a ZCS is expected to arise. Figure 6(e) shows that the expected ZCS is embedded in the bulk continuum due to the absence of a band gap at zero energy. In order to avoid numerical complication that the ZCS wave function gets generally mixed with other degenerate bulk states, we adopt the method used in Ref. [47]:

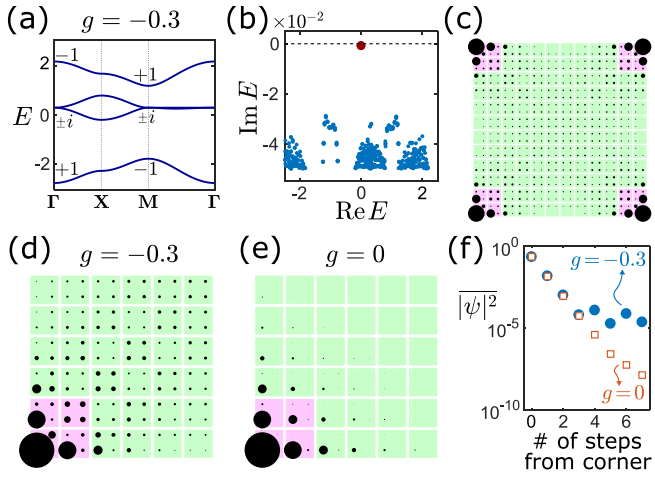

FIG. 7. (a) Band structure of a chiral-symmetry-broken $h^{(4)}$ structure along with C_4-rotation eigenvalues at Γ and M; $t = -0.25$, $\lambda = -1$, and $g = -0.3$. (b) Eigenvalues in a complex energy plane obtained by using the same setting described in Fig. 6(f). (c) Field profile of the modes marked as dark red dots in (b). (d) Zoom on one of the quadrants of (c). (e) Zoom on one of the quadrants of a ZCS wave function, Fig. 6(h). (f) Average wave function amplitude $\overline{|\psi|^2}$ in a unit cell as a function of the number of grid steps $(x + y)$ from the cornermost unit cell.

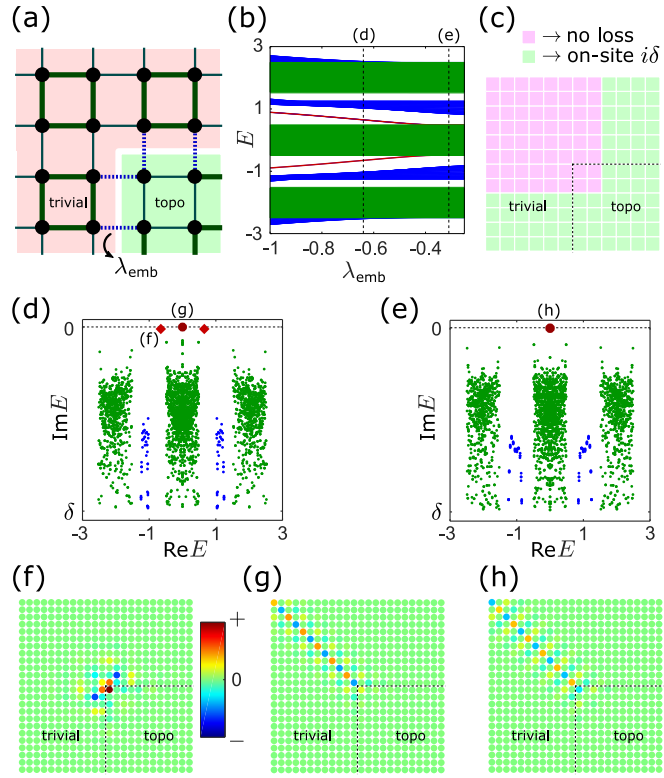

FIG. 8. (a) Embedded corner between a topological domain and a trivial domain; λ_{emb} refers to the coupling strength of the hopping across the domains. (b) Spectral flow, with varying λ_{emb}, of the embedded structure with a finite size (10 by 10 unit cells of the topological domain surrounded by the trivial domain of 5 unit-cell-long thickness); the green areas refer to bulk modes, the blue lines are edge(domain wall)-localized modes, and the dark red lines denote the corner localized states. (c) Similar to Fig. 6(f), a uniform on-site loss of δ is introduced except around the embedded corner. (d) Resulting complex eigenvalues with $\lambda_{emb} = -0.64$. (e) Complex eigenvalues with $\lambda_{emb} = -0.31$. (f) Field profile of the embedded corner state [marked as a red diamond in (d)]. (g), (h) Field profile of ZCSs delocalized toward the outer trivial domain [marked as dark red dots in (d), (e)].

as shown in Fig. 6(f), we introduced a uniform loss of $i\delta$ ($\delta = -0.05$) in the system except at small subsystems (2×2 unit cell) at each corner. Then, the corner-localized states will be easily identified, as their imaginary part of eigenvalue becomes much smaller than other bulk modes; see Fig. 6(g). As expected, Fig. 6(h) clearly shows the wave function of a truly corner-localized zero energy state at each corner.

The diagonal hopping across diagonally adjacent unit cells g, see Fig. 2(b), can be used to remove the chiral symmetry while preserving C_{4v} symmetry. Since C_4 symmetry is preserved, the perturbed structure with a finite g still inherits the same C_4- and C_2-rotation eigenvalues for the modes at rotation-invariant momenta, given that g is not too large to cause band inversion. In other words, a moderate strength of g does not change bulk topological invariants $\mathbf{p}$ and Q_c that are discussed in the previous section. Figure 7(a) shows that a finite g breaks the chiral symmetry, as seen in the band structure that is not mirror symmetric around the zero energy. Then, we observe that the modes that were ZCSs with $g = 0$ now get hybridized with the bulk continuum due to broken chiral symmetry. A detailed analysis on how this hybridization occurs as a result of chiral symmetry breaking is provided in Ref. [47]. Figures 7(c)–7(f) show that the wave function amplitude of these hybridized modes remains finite in the bulk unlike the true ZCS wave function which decays exponentially from the corner. This observation verifies that the presence of the chiral symmetry with respect to zero energy plays a pivotal role in the existence of a ZCS, in agreement both with Ref. [47] and our BBC established above.

V. C_4-SYMMETRIC TCI WITH EMBEDDED BOUNDARIES

As we discussed earlier, there have been several works that studied the corner states in C_4 TCI at an embedded corner interfaced with a surrounding trivial domain [35–43], where these corner states emerge in the band gap between the first and the second bands instead of at zero energy. These studies labeled such corner states to be *second-order topological* simply because the nonzero bulk polarization coappears with the corner states, or conflated the origin of their corner state with that of the topological ZCS studied in this work without enough justification [35]. Here, however, we provide a detailed explanation on why the embedded corner states reported in Refs. [35–43] are trivial defect states, sharing no commonality in their formation mechanism with the ZCS studied in the previous section and in Refs. [47,48].

Figure 8(a) depicts the geometry of the topological domain ($|t| = 0.25 < |\lambda| = 1$) interfacing with the trivial domain ($|t| = 1 > |\lambda| = 0.25$) around an embedded corner. Naturally, the coupling strength of the hopping across the domains, λ_{emb}, would be given as a free parameter, which is determined by the microscopic details of the system and not by any topological

effects. In the ring-resonator-based [13] or circuit-based [14] waveguide flatforms, the system can be designed for any arbitrary strength of interdomain coupling λ_{emb}. In the photonic crystal structures with subwavelength periodicities [35,36], we can reasonably expect that the strength of λ_{emb} would fall in the range between two λ values in the trivial domain and the topological domain.

In Fig. 8(b), we computed the spectral flow of the embedded structure with a finite size, as λ_{emb} is varied between -1 (λ in the topological domain) and -0.25 (λ in the trivial domain). The red curves correspond to the embedded corner state predicted and observed in Refs. [35–43]. In a certain range ($|\lambda_{emb}| < 0.4$ in this example), these embedded corner states are completely lost, even though C_{4v} symmetries of each bulk domain, the bulk polarization of each domain, and the chiral symmetry of the entire system are not changing. Figures 8(d) and 8(e) also depict that these states (red diamond) are not topologically protected in their spectral positions, get drifted, and disappear as λ_{emb} varies. Note that we did not even resort to any extreme or artificial choice in the value of λ_{emb} in order to demonstrate the fragility of this embedded corner state; as stated above, we only considered the range of λ_{emb} to fall between two λ values in the trivial domain and the topological domain. Therefore, these states are trivial defect states, not protected by any crystalline symmetries nor by the bulk polarization. In fact, the field profile of this embedded-corner state calculated from our tight-binding model, see Fig. 8(f), is nearly identical to the field profiles reported in the above-mentioned works [35–43]. Figures 8(f) and 8(g) then show the field profile of the zero-energy states that correspond to the ZCSs in the open-boundary system. These states reduce back to the ZCSs in Fig. 6(h) in the limit of $\lambda_{emb} \to 0$. Because the outer domain is also gapless around the zero energy, the ZCS of the inner domain appears as delocalized toward the outer trivial domain, even though it remains exponentially localized toward the inner topological domain.

VI. CONCLUSION

In conclusion, we addressed that a topological correspondence between a corner state and a nontrivial bulk invariant should be claimed by a physical argument (e.g., a half charge with chiral symmetry), but not by coincidence of their existence conditions in terms of the Hamiltonian parameters. We revealed that the corner states that claimed to be *second-order topological* in the above-mentioned works regarding the breathing Kagome lattice [21–34] or regarding the two-dimensional SSH model [35–43] turn out to have no connection to any bulk topology despite the shared phase boundaries in the Hamiltonian parameter spaces with the bulk polarization. Therefore, our examples in these two-dimensional C_3- and C_4-symmetric crystalline insulators clearly demonstrated that the bulk polarization, which has a well-established causal relationship with the fractional corner charge anomaly, cannot be attributed to the emergence of the corner states at zero energy in general. In addition, we refined the bulk-corner correspondences for the corner states in these examples by identifying other topological invariants that are truly responsible for the corner state formation.

ACKNOWLEDGMENTS

We thank Dr. A. Cerjan for clarifying discussion regarding Ref. [47]. This work was supported by the Office of Naval Research (ONR) under Grant No. N00014-21-1-2056 and by the National Science Foundation (NSF) under Grants No. DMR-1741788 and No. DMR-1719875. M.J. was also supported in part by the Kwanjeong Fellowship from Kwanjeong Educational Foundation.

APPENDIX

Exact mapping of the edge-localized band in Fig. 3(f) onto a chiral-symmetric SSH chain

Here we show how the edge-localized band of a 1D-periodic nanoribbon structure out of a breathing Kagome lattice can be exactly mapped onto a chiral-symmetric 1D SSH model. We also explain why the chiral-partner band does not appear in the same band structure.

The 1D SSH model is described by the following Hamiltonian:

$$\mathcal{H}_{\rm SSH} = \sum_{n\in\mathbb{Z}} (t\hat{c}^\dagger_{A,n\mathbf{R}_1}\hat{c}_{B,n\mathbf{R}_1} + \lambda\hat{c}^\dagger_{A,n\mathbf{R}_1}\hat{c}_{B,(n-1)\mathbf{R}_1} + \text{c.c.}), \quad \text{(A1)}$$

where $\mathbf{R}_1$ is the primitive lattice vector and $\hat{c}_{A/B,\mathbf{R}}$ and $\hat{c}^\dagger_{A/B,\mathbf{R}}$ are the annihilation and creation operators for the sublattice A/B in the unit cell located at $\mathbf{R}$. By introducing the momentum space operators, $\hat{c}_{A/B,k_{1d}} = \frac{1}{\sqrt{L}}\sum_{n\in\mathbb{Z}} e^{-ink_{1d}}\hat{c}_{A/B,n\mathbf{R}_1}$ (L: the total length of SSH chain; $k_{1d} = \mathbf{k}\cdot\mathbf{R}_1$, where $\mathbf{k}$ is the Bloch momentum), we can obtain the momentum space Hamiltonian $H(k_{1d})$:

$$\mathcal{H}_{\rm SSH} = \sum_{k_{1d}\in[-\pi,\pi)} \begin{bmatrix}\hat{c}^\dagger_{A,k_{1d}} & \hat{c}^\dagger_{B,k_{1d}}\end{bmatrix} H(k_{1d}) \begin{bmatrix}\hat{c}_{A,k_{1d}} \\ \hat{c}_{B,k_{1d}}\end{bmatrix}, \quad \text{(A2a)}$$

$$H(k_{1d}) = \begin{bmatrix} 0 & t+\lambda\, e^{-ik_{1d}} \\ t+\lambda\, e^{ik_{1d}} & 0\end{bmatrix}. \quad \text{(A2b)}$$

This Hamiltonian in Eq. (A2b) is solved $H(k_{1d})\vec{v}_\pm = E_\pm\vec{v}_\pm$ as below:

$$E_\pm(k_{1d}) = \pm\text{sgn}(t)\sqrt{t^2+\lambda^2+2t\lambda\,\cos(k_{1d})}, \quad \text{(A3a)}$$

$$\vec{v}_\pm(k_{1d}) = \frac{1}{\sqrt{2}}[\alpha_\pm(k_{1d})1]^\dagger, \quad \text{(A3b)}$$

$$\alpha_\pm(k_{1d}) = \pm\frac{\sqrt{|t|+|\lambda|e^{ik_{1d}}}}{\sqrt{|t|+|\lambda|e^{-ik_{1d}}}}. \quad \text{(A3c)}$$

Therefore, we get the following eigenbasis of $\mathcal{H}_{\rm SSH}$: $\mathcal{H}_{\rm SSH}\,|k_{1d};\pm\rangle = E_\pm(k_{1d})\,|k_{1d};\pm\rangle$, where

$$|k_{1d};\pm\rangle = \frac{1}{\sqrt{2}}[\alpha_\pm(k_{1d})\hat{c}^\dagger_{A,k_{1d}} + \hat{c}^\dagger_{B,k_{1d}}]\,|\text{vac}\rangle\,. \quad \text{(A4)}$$

Now, let us turn to the breathing Kagome lattice shown in Fig. 2(a). Consider edge-localized modes along an edge terminated by the side parallel to $\mathbf{R}_1$ drawn in Fig. 3(a). Let us label the two sublattices along the terminated edge as A and B, and the other third sublattice as C. Then, the Hamiltonian for this edge-terminated Kagome lattice is given

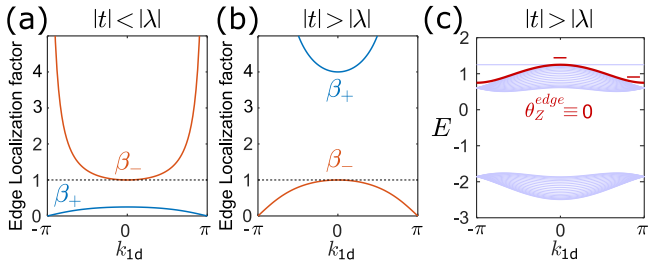

FIG. 9. $\beta_{\pm}(k_{1d})$ in Eq. (A7) calculated (a) with $t = -0.25$ and $\lambda = -1$ and (b) with $t = -1$ and $\lambda = -0.25$. (c) Edge dispersion with $t = -1$ and $\lambda = -0.25$ of nanoribbon structure with an edge termination like one of the edges in Fig. 3(a); the edge localized band is colored red along with its inversion eigenvalues at high symmetry points.

as

$$\begin{aligned}\mathcal{H}_{\text{edge}} = \sum_{n\in\mathbb{Z},m\geqslant 0} & (t\hat{c}^{\dagger}_{A,n\mathbf{R}_1+m\mathbf{R}_2}\hat{c}_{B,n\mathbf{R}_1+m\mathbf{R}_2} \\ & + t\hat{c}^{\dagger}_{B,n\mathbf{R}_1+m\mathbf{R}_2}\hat{c}_{C,n\mathbf{R}_1+m\mathbf{R}_2} \\ & + t\hat{c}^{\dagger}_{C,n\mathbf{R}_1+m\mathbf{R}_2}\hat{c}_{A,n\mathbf{R}_1+m\mathbf{R}_2} \\ & + \lambda\hat{c}^{\dagger}_{A,n\mathbf{R}_1+m\mathbf{R}_2}\hat{c}_{B,(n-1)\mathbf{R}_1+m\mathbf{R}_2} \\ & + \lambda\hat{c}^{\dagger}_{B,n\mathbf{R}_1+(m+1)\mathbf{R}_2}\hat{c}_{C,(n+1)\mathbf{R}_1+m\mathbf{R}_2} \\ & + \lambda\hat{c}^{\dagger}_{C,n\mathbf{R}_1+m\mathbf{R}_2}\hat{c}_{A,n\mathbf{R}_1+(m+1)\mathbf{R}_2} + \text{c.c.}), \end{aligned} \tag{A5}$$

where $\mathbf{R}_2$ is the other primitive lattice vector that is not parallel to the terminated edge; see Fig. 3(a). In order to map these edge-localized modes to 1D SSH eigenstates in Eq. (A4), let us take the following ansatz:

$$|k_{1d};\pm\rangle = [\alpha_{\pm}(k_{1d})\hat{c}^{\dagger}_{A,k_{1d};\pm} + \hat{c}^{\dagger}_{B,k_{1d};\pm}]\,|\text{vac}\rangle\,, \tag{A6a}$$

$$\hat{c}_{A/B,k_{1d};\pm} = \sum_{n\in\mathbb{Z},m\geqslant 0} [\beta_{\pm}(k_{1d})]^m e^{-ink_{1d}}\hat{c}_{A/B,n\mathbf{R}_1+m\mathbf{R}_2}. \tag{A6b}$$

Here, $\alpha_{\pm}(k_{1d})$ takes the same expression to Eq. (A3c) and $\beta_{\pm}(k_{1d})$ signifies the edge localization. A proper normalization factor is not considered in Eqs. (A6) for now, but this does not affect any of the following discussions. As we enforce $\mathcal{H}_{\text{edge}}\,|k_{1d};\pm\rangle = E_{\pm}(k_{1d})\,|k_{1d};\pm\rangle$, the wave function amplitudes on every sublattice C are required to vanish and we obtain the following expression for the edge localization factor:

$$\beta_{\pm}(k_{1d}) = \frac{t}{\lambda}\frac{1+\alpha_{\pm}(k_{1d})}{1+\alpha_{\pm}(k_{1d})e^{-ik_{1d}}}. \tag{A7}$$

In order for the modes in Eq. (A6a) to be truly edge localized, the norm of β should be less than 1. In fact, if we have $\lambda < t < 0$ ($|t| < |\lambda|$) as in the main text, we get $|\beta_+(k_{1d})| < 1 \leqslant |\beta_-(k_{1d})|$; see Fig. 9(a).

Therefore, the ansatz $|k_{1d};+\rangle$ is a valid eigenstate for $\mathcal{H}_{\text{Edge}}$ with proper edge localization, and this is the exact solution that describes the edge-localized band in Fig. 3(f) with dispersion relation of $E_+(k_{1d})$ from Eq. (A3a). The chiral partner band $E_-(k_{1d})$ does not appear in the edge band dispersion, since $|k_{1d};-\rangle$ states violate the edge localization condition $|\beta_-(k_{1d})| \geqslant 1$. The same analysis can be repeated for more generic cases as depicted in Fig. 5(a), where all the hopping strengths $t/\lambda_{1,2,3}$ are different, and the edge localized band with a proper mapping onto a 1D SSH chain can be found as long as $|t_i| < |\lambda_i|$ is met for each $i = 1, 2$. t_3 and λ_3 do not play any role in determining the existence of a ZCS at the corner made by edges along $\mathbf{R}_1$ and $\mathbf{R}_2$.

Lastly, we note that the breathing Kagome lattice with $|t| > |\lambda|$ (no bulk polarization) still supports an edge-localized band. Figure 9(b) shows the edge localization factors for this trivial case $|t| > |\lambda|$; $|\beta_-(k_{1d})| \leqslant 1 < |\beta_+(k_{1d})|$. Thus, in the same way, the ansatz $|k_{1d};-\rangle$ is a valid eigenstate for $\mathcal{H}_{\text{edge}}$ with proper edge localization, and this is the exact solution that describes the edge-localized band in Fig. 9(c) with dispersion relation of $E_-(k_{1d})$ from Eq. (A3a). This edge-mapped SSH chain features a trivial (vanishing) Zak phase, as the inversion eigenvalues at $k_{1d} = 0, \pi$ are equally -1.

[1] A. P. Schnyder, S. Ryu, A. Furusaki, and A. W. W. Ludwig, Phys. Rev. B **78**, 195125 (2008).
[2] S. Ryu, A. P. Schnyder, A. Furusaki, and A. W. W. Ludwig, New J. Phys. **12**, 065010 (2010).
[3] L. Fidkowski, T. S. Jackson, and I. Klich, Phys. Rev. Lett. **107**, 036601 (2011).
[4] G. M. Graf and M. Porta, Commun. Math. Phys. **324**, 851 (2013).
[5] K. Shiozaki and M. Sato, Phys. Rev. B **90**, 165114 (2014).
[6] M. Sitte, A. Rosch, E. Altman, and L. Fritz, Phys. Rev. Lett. **108**, 126807 (2012).
[7] W. A. Benalcazar, B. A. Bernevig, and T. L. Hughes, Science **357**, 61 (2017).
[8] Z. Song, Z. Fang, and C. Fang, Phys. Rev. Lett. **119**, 246402 (2017).
[9] J. Langbehn, Y. Peng, L. Trifunovic, F. von Oppen, and P. W. Brouwer, Phys. Rev. Lett. **119**, 246401 (2017).
[10] F. Schindler, A. M. Cook, M. G. Vergniory, Z. Wang, S. S. P. Parkin, B. A. Bernevig, and T. Neupert, Sci. Adv. **4**, eaat0346 (2018).
[11] W. A. Benalcazar, B. A. Bernevig, and T. L. Hughes, Phys. Rev. B **96**, 245115 (2017).
[12] F. Schindler, Z. Wang, M. G. Vergniory, A. M. Cook, A. Murani, S. Sengupta, A. Y. Kasumov, R. Deblock, S. Jeon, I. Drozdov, H. Bouchiat, S. Guéron, A. Yazdani, B. A. Bernevig, and T. Neupert, Nat. Phys. **14**, 918 (2018).
[13] J. Noh, W. A. Benalcazar, S. Huang, M. J. Collins, K. P. Chen, T. L. Hughes, and M. C. Rechtsman, Nat. Photon. **12**, 408 (2018).
[14] C. W. Peterson, W. A. Benalcazar, T. L. Hughes, and G. Bahl, Nature (London) **555**, 346 (2018).
[15] M. Serra-Garcia, V. Peri, R. Süsstrunk, O. R. Bilal, T. Larsen, L. G. Villanueva, and S. D. Huber, Nature (London) **555**, 342 (2018).
[16] S. Mittal, V. V. Orre, G. Zhu, M. A. Gorlach, A. Poddubny, and M. Hafezi, Nat. Photon. **13**, 692 (2019).
[17] M. Geier, L. Trifunovic, M. Hoskam, and P. W. Brouwer, Phys. Rev. B **97**, 205135 (2018).
[18] L. Trifunovic and P. W. Brouwer, Phys. Rev. X **9**, 011012 (2019).

[19] R. Takahashi, Y. Tanaka, and S. Murakami, Phys. Rev. Research **2**, 013300 (2020).
[20] D. J. Thouless, M. Kohmoto, M. P. Nightingale, and M. denNijs, Phys. Rev. Lett. **49**, 405 (1982).
[21] M. Ezawa, Phys. Rev. Lett. **120**, 026801 (2018).
[22] X. Ni, M. Weiner, A. Alu, and A. B. Khanikaev, Nat. Mater. **18**, 113 (2019).
[23] H. Xue, Y. Yang, F. Gao, Y. Chong, and B. Zhang, Nat. Mater. **18**, 108 (2019).
[24] S. N. Kempkes, M. R. Slot, J. J. van den Broeke, P. Capiod, W. A. Benalcazar, D. Vanmaekelbergh, D. Bercioux, I. Swart, and C. M. Smith, Nat. Mater. **18**, 1292 (2019).
[25] H. Yang, Z.-X. Li, Y. Liu, Y. Cao, and P. Yan, Phys. Rev. Research **2**, 022028(R) (2020).
[26] M. Weiner, X. Ni, M. Li, A. Alu, and A. B. Khanikaev, Sci. Adv. **6**, eaay4166 (2020).
[27] M. Li, D. Zhirihin, M. Gorlach, X. Ni, D. Filonov, A. Slobozhanyuk, A. Alù, and A. B. Khanikaev, Nat. Photon. **14**, 89 (2020).
[28] H. Wakao, T. Yoshida, H. Araki, T. Mizoguchi, and Y. Hatsugai, Phys. Rev. B **101**, 094107 (2020).
[29] A. Vakulenko, S. Kiriushechkina, M. Wang, M. Li, D. Zhirihin, X. Ni, S. Guddala, D. Korobkin, A. Alù, and A. B. Khanikaev, Adv. Mater. **33**, 2004376 (2021).
[30] Y. Chen, X. Lu, and H. Chen, Opt. Lett. **44**, 4251 (2019).
[31] L. Song, H. Yang, Y. Cao, and P. Yan, Nano Lett. **20**, 7566 (2020).
[32] K. Kudo, T. Yoshida, and Y. Hatsugai, Phys. Rev. Lett. **123**, 196402 (2019).
[33] H. Xue, Y. Yang, G. Liu, F. Gao, Y. Chong, and B. Zhang, Phys. Rev. Lett. **122**, 244301 (2019).
[34] Z. Li, Y. Cao, P. Yan, and X. Wang, npj Comput. Mater. **5**, 107 (2019).
[35] B.-Y. Xie, H.-F. Wang, H.-X. Wang, X.-Y. Zhu, J.-H. Jiang, M.-H. Lu, and Y.-F. Chen, Phys. Rev. B **98**, 205147 (2018).
[36] X.-D. Chen, W.-M. Deng, F.-L. Shi, F.-L. Zhao, M. Chen, and J.-W. Dong, Phys. Rev. Lett. **122**, 233902 (2019).
[37] Z. Zhang, H. Long, C. Liu, C. Shao, Y. Cheng, X. Liu, and J. Christensen, Adv. Mater. **31**, 1904682 (2019).
[38] Y. Ota, F. Liu, R. Katsumi, K. Watanabe, K. Wakabayashi, Y. Arakawa, and S. Iwamoto, Optica **6**, 786 (2019).
[39] B.-Y. Xie, G.-X. Su, H.-F. Wang, H. Su, X.-P. Shen, P. Zhan, M.-H. Lu, Z.-L. Wang, and Y.-F. Chen, Phys. Rev. Lett. **122**, 233903 (2019).
[40] M. Kim and J. Rho, Nanophotonics **9**, 3227 (2020).
[41] X. Xie, W. Zhang, X. He, S. Wu, J. Dang, K. Peng, F. Song, L. Yang, H. Ni, Z. Niu, C. Wang, K. Jin, X. Zhang, and X. Xu, Nanophotonics **14**, 1900425 (2020).
[42] W. Zhang, X. Xie, H. Hao, J. Dang, S. Xiao, S. Shi, H. Ni, Z. Niu, C. Wang, K. Jin, X. Zhang, and X. Xu, Light Sci. Appl. **9**, 109 (2020).
[43] C. Han, M. Kang, and H. Jeon, ACS Photon. **7**, 2027 (2020).
[44] Z. Zhang, M. Rosendo Lopez, Y. Cheng, X. Liu, and J. Christensen, Phys. Rev. Lett. **122**, 195501 (2019).
[45] T. Liu, Y.-R. Zhang, Q. Ai, Z. Gong, K. Kawabata, M. Ueda, and F. Nori, Phys. Rev. Lett. **122**, 076801 (2019).
[46] W. A. Benalcazar, T. Li, and T. L. Hughes, Phys. Rev. B **99**, 245151 (2019).
[47] W. A. Benalcazar and A. Cerjan, Phys. Rev. B **101**, 161116(R) (2020).
[48] A. Cerjan, M. Jurgensen, W. A. Benalcazar, S. Mukherjee, and M. C. Rechtsman, Phys. Rev. Lett. **125**, 213901 (2020).
[49] Y. Hatsugai, Phys. Rev. Lett. **71**, 3697 (1993).
[50] G. van Miert and C. Ortix, Phys. Rev. B **96**, 235130 (2017).
[51] C. W. Peterson, T. Li, W. A. Benalcazar, T. L. Hughes, and G. Bahl, Science **368**, 1114 (2020).
[52] M. Xiao, G. Ma, Z. Yang, P. Sheng, Z. Q. Zhang, and C. T. Chan, Nat. Phys. **11**, 240 (2015).
[53] Z. Fan, S. Dutta-Gupta, R. Gladstone, S. Trendafilov, M. Bosch, M. Jung, G. R. S. Iyer, A. J. Giles, M. Shcherbakov, B. Feigelson, J. D. Caldwell, M. Allen, J. Allen, and G. Shvets, Nanophotonics **8**, 1417 (2019).
[54] T. I. Tuegel, V. Chua, and T. L. Hughes, Phys. Rev. B **100**, 115126 (2019).
[55] L. He, Z. Addison, E. J. Mele, and B. Zhen, Nat. Commun. **11**, 3119 (2020).
[56] M. Jung, R. Gladstone, and G. Shvets, Adv. Photon. **2**, 46003 (2020).